

# Mesoscale eddies and submesoscale structures of Persian Gulf Water off the Omani coast in Spring 2011

Pierre L'Hégaret <sup>\*1</sup>, Xavier Carton<sup>1</sup>, Stephanie Louazel<sup>2</sup>, and Guillaume Boutin<sup>1</sup>

<sup>1</sup>Laboratoire de Physique des Océans/UMR6523, UBO, 6 avenue Le Gorgeu CS93837,  
29238 Brest cedex 3, France

<sup>2</sup>Service Hydrographique et Oceanographique de la Marine, 13 rue de Chatellier  
CS92803, 29228 Brest cedex 2, Brest, France

April 8, 2016

## 1 Abstract

The Persian Gulf produces a high salinity water (Persian Gulf Water, PGW hereafter), which flows into the Sea of Oman via the Strait of Hormuz. Beyond the Strait of Hormuz, the PGW cascades down the continental slope and spreads in the Sea of Oman under the influence of the energetic mesoscale eddies. The PGW outflow has different thermohaline characteristics and pathways depending of the season. In spring 2011, the Phys-Indien experiment was carried out in the Arabian Sea and in the Sea of Oman. The Phys-Indien 2011 measurements, as well as satellite observations, are used here to characterize the circulation induced by the eddy field and its impact on the PGW pathway and evolution. During the spring intermonsoon, an anticyclonic eddy is often observed at the mouth of the Sea of Oman. This structure was observed in 2011. It creates a front between the eastern and western part of the basin. Two energetic eddies were also present along the southern Omani coast in the Arabian Sea. At their peripheries, ribbons of fresh and cold water were found due to the stirring created by the eddies. The PGW characteristics is strongly influenced by these eddies. In the western Sea of Oman, the PGW was fragmented into filaments and submesoscale eddies. It also recirculated locally, thus creating salty layers with different densities. In the Arabian Sea, a highly saline submesoscale lens was recorded offshore. Its characteristics are analysed here and possible origins are proposed. The recurrence of such lenses in the Arabian Sea is also briefly examined.

## 2 Introduction

The Indian Ocean, the third tropical basin in size, is bounded to the north by the Asian landmass. This landmass leads to the existence of monsoons, which strongly influence the regional oceanic circulation. The northwestern part of the Indian Ocean is comprised of different sub-basins, each with specific geographic and climatic characteristics. This study focuses on two of them, the Sea of Oman (or Gulf of Oman) and the Arabian Sea (see figure 1). The Sea of Oman connects the Persian Gulf to the Arabian Sea; this sea deepens and widens along its zonal axis, from the Strait of Hormuz to its mouth, at Ra's Al Hadd. The northwestern Arabian Sea has a bottom below 3500 m depth, and a narrow continental shelf, which widens only from Ra's Al Hadd to Ra's Madrasah along the Omani coast; its depth is 200 m (see again figure 1 for locations). The Arabian Sea is also crossed by the Owen Fracture Zone from north-east to south-west, with diving and rising of the seafloor along the fault.

The surface circulation around the Arabian Peninsula is forced by the atmospheric monsoon cycle. During the Southwest monsoon, in summer, strong and steady southwestern winds run across the basin

---

\*pierre.lhegaret@outlook.com

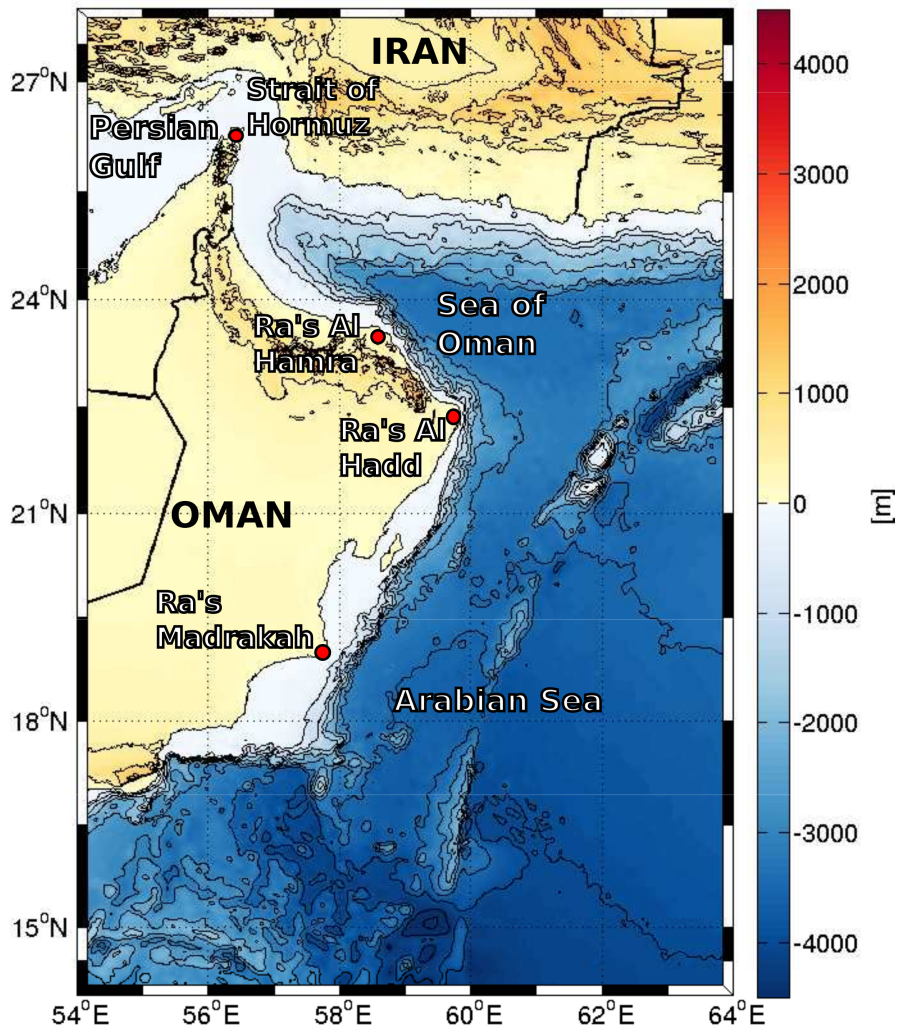


Figure 1: Topographic map of the Arabian Sea and Sea of Oman with the locations of interest.

39 (see Findlater (1969)); they reverse in winter, during the Northeast monsoon, with also steady but weaker  
40 winds. The inter monsoons, in spring and fall, are marked with a decrease in winds intensity and a loss  
41 of preferred direction.

42 The upper ocean response is highly variable spatially and seasonally. In summer (winter), alongshore  
43 currents extend along a "belt", with negative (positive) sea level anomaly along the western and northern  
44 coasts. These anomalies grow under the influence of the monsoon wind stress, associated with upwellings  
45 (downwellings) (see Lee et al. (2000)). These currents then destabilize to form meanders and mesoscale  
46 eddies with a radius comparable with, or slightly larger than, the first baroclinic radius of deformation  
47 (about 40 km in the region, see Chelton et al. (1998)). These eddies are known to dominate the near  
48 surface circulation offshore (see Fischer et al. (2002)) and to induce horizontal transports. They have a  
49 vertical influence on the water masses at depth (see Bower and Furey (2012) and Carton et al. (2012)).  
50 Other processes can lead to the formation of such eddies, depending on the location and the season.  
51 Al Saafani et al. (2007) identified eddies in the Gulf of Aden, generated by Rossby waves emitted from  
52 the Indian coast or amplified in the interior of the basin. This mechanism is also present in the northern  
53 Arabian Sea, with Rossby waves being forced by wind and by coastal Kelvin waves (see L'Hégaret et al.  
54 (2015)).

55 Over the Persian Gulf, steady winds and solar heating lead to intense evaporation (see Privett (1959)  
56 and Meshal and Hassan (1986)); this region also has little fresh water inflow (through precipitation and  
57 river, see Reynolds (1993)); the large deficit of precipitation (or river inflow) over evaporation results in  
58 the formation of highly saline water in the Persian Gulf. This water mass, called PGW (Persian Gulf  
59 Water), with salinity above 40 psu, flows into the Sea of Oman via the Strait of Hormuz. The density  
60 of the outflowing PGW varies seasonally, densest water being formed in winter Swift and Bower (2003).  
61 In the Sea of Oman, the PGW outflow equilibrates around 250 meters depth, mixing with the fresher  
62 Indian Ocean Central Water (IOCW). Another salty water mass, the Arabian Sea High Salinity Water  
63 (ASHSW), with salinity above 36.6 psu, forms in the Arabian Sea in winter (see Kumar and Prasad  
64 (1999)), and occupies the upper part of the water column.

65 In the past, few dedicated cruises provided observations to describe the PGW pathway out of the  
66 Persian Gulf, and its variations in the Sea of Oman. The PGW outflow was usually presented as  
67 a southeastward flow, along the coast of Oman (see Premchand et al. (1986)). Indeed, in October-  
68 November 1999, during the fall inter-monsoon, the GOGP99 experiment at sea sampled the PGW  
69 outflow and identified it as a coastal flow, extending to the southern coast of Oman (see Pous et al.  
70 (2004)). During other seasons, the path of the PGW in the Gulf of Oman is less regular, as shown by  
71 observations and by numerical modeling; also, PGW can exit under the form of short pulses (see Banse  
72 (1997), Senjyu et al. (1998), Bower et al. (2000), Prasad et al. (2001), Thoppil and Hogan (2009), Wang  
73 et al. (2012) and Wang et al. (2013)). Recently, ARGO floats (see Carton et al. (2012) and L'Hégaret  
74 et al. (2013)), and HYCOM numerical simulations (see L'Hégaret et al. (2015)), confirmed that during  
75 other seasons, PGW can be expelled from the coast into the sea of Oman. These ejections were related  
76 to the presence of mesoscale eddies in the Sea of Oman, and especially to the presence of a dipole in  
77 spring; different offshore mechanisms were identified. PGW ejection was also identified in response to  
78 tropical atmospheric cyclone (in particular cyclone Gonu; Wang et al. (2012), Wang et al. (2013)).

79 In spring 2011, the Phys-Indien experiment was carried out around the Arabian Peninsula, recording  
80 the thermohaline and dynamical characteristics of the upper ocean. Mesoscale surface eddies, and sub-  
81 mesoscale fragments of PGW, were sampled in the Sea of Oman and off Ra's Al Hadd, in the Arabian  
82 Sea.

83 This objective of this paper is twofold. First, it will describe the mesoscale surface eddies in spring  
84 2011 and how they advect the surrounding water masses. Second, it will present the structure and  
85 possible recurrence of submesoscale PGW fragments, in particular those embedded in mesoscale eddies.  
86 To achieve these objectives, in-situ data collected during the Phys-Indien experiment and satellite mea-  
87 surements will be used. The altimetric data provide temporal continuity to study the evolution of the  
88 mesoscale features (but with a low spatial resolution). The in-situ observations give a finer scale, but  
89 instantaneous, description of the eddies and water masses.

90

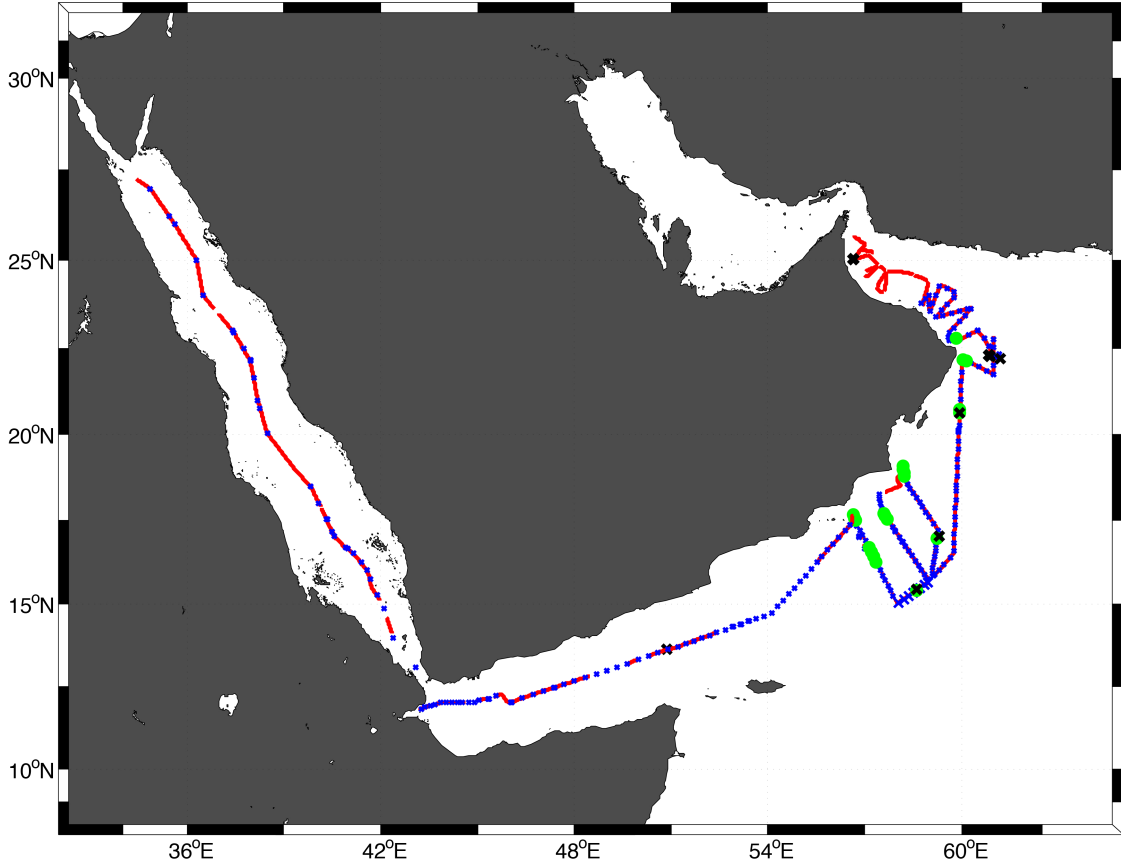


Figure 2: Location of the Phys-Indien 2011 measurements. The red line follows the VM-ADCP and SeaSoar lines (with the exception of the Red Sea and Gulf of Aden where only the VM-ADCP was activated). The blue crosses and green circles represent the positions of XBT-XCTD casts and of CTDL-ADCP stations respectively. The black crosses represent the launch positions of floats (Surdrift and PROVOR).

## 2.1 The Phys-Indien 2011 measurements

The Phys-Indien 2011 experiment measured the circulation and water masses in the sub-basins around the Arabian Peninsula, from the Red Sea to the Persian Gulf, starting in late February until April 2011; it relied on various devices: two CTD probes on a SeaSoar, a CTD and a lowered ADCP at stations, XBT and XCTD probes, VM-ADCP, Surdrift buoys and profiling floats, meteorological sensors. The Phys-Indien sections are shown on figure 2. This study focuses on the measurements in the northwestern Arabian Sea and in the Sea of Oman, in March 2011. In particular, these sections crossed mesoscale eddies and the PGW outflow and fragments.

On the SeaSoar sections, pressure, temperature and conductivity were measured in the upper 350 meters of the water column with accuracies of  $10^{-3}$  °C,  $3 \cdot 10^{-4}$  S.m<sup>-1</sup> and 0.015% of the pressure value. Salinity was calculated from temperature and conductivity. In this region, strong horizontal and vertical thermohaline gradients occur, which can lead to biases in temperature and salinity measurements by seaSoars. These biases are due to thermal inertia of the sensors, and mostly occur between the lowering and rising of the device, which result in a delay between the conductivity and temperature measurements (see Barth et al. (1996)). These errors were corrected by applying a couple of coefficients, a first one correcting the amplitude of the signals between the rising and the lowering of the SeaSoar, and a second coefficient correcting the time delay (see Lueck and Picklo (1990)). Once corrected, the SeaSoar measurements were validated against CTD station or XCTD casts data (such stations or casts were achieved along the SeaSoar transects). The relative residual error of the corrected SeaSoar salinity

111 remains below 0.5%, at the CTD stations.

112 The horizontal velocity was obtained with a 38 kHz Vessel Mounted - ADCP (VM-ADCP hereafter);  
 113 this device measures currents from the surface to about 1000 meter depth; the depth range depends on  
 114 the matter in suspension in seawater, which can reflect the acoustic signal. In a few occurrences, currents  
 115 could be measured down to 1600 m depth. The accuracy of VM-ADCP on the horizontal components of  
 116 velocity, is of  $5 \cdot 10^{-3} \text{ m.s}^{-1}$ . VM-ADCP provides high resolution measurements but is sensitive to noise  
 117 due to biological activity. Here, a low pass filter was applied to the signal, keeping the structures with a  
 118 size larger than 3 km, to focus on the submesoscale and mesoscale processes. Another VM-ADCP, with  
 119 150 kHz frequency, was activated but its data are not shown here (due to too shallow a reach). These  
 120 data were used nevertheless to validate the 38 kHz ADCP measurements in the upper ocean. A few  
 121 VM-ADCP sections were interrupted or were too noisy, thus leading to blanks. No interpolation was  
 122 carried out and the blanks are displayed on the figures. Blanks (due to interruptions) can also appear  
 123 on a few of the SeaSoar transects.

124 During Phys-Indien, five drogued Surdrift buoys were deployed and programmed for 180 days of  
 125 recording. These surface buoys were connected to a large holey-sock drogue by a thin Kevlar cable,  
 126 80 to 250 m long. A test on the acceleration of each buoy was applied to determine a possible loss of  
 127 the drogue. These buoys were positioned by Argos, their trajectories were sampled every hour and a  
 128 thermistor sensor gave the surface temperature at each recording.

129 Also, 6 PROVOR floats were deployed during this cruise. They were positioned via Argos when  
 130 they surfaced at the end of each 5-day cycle. These floats were equipped with a CTD probe providing  
 131 temperature, conductivity and pressure with an accuracy of  $0.01^\circ\text{C}$ ,  $10^{-3} \text{ S.m}^{-1}$  and 1 dbar respectively.  
 132 Their parking depth was programmed to 700 dbar (instead of the usual 1000 dbar); they dived to 2000  
 133 dbar every 5 days and acquired data while rising to the surface, where these data were transmitted.

## 134 2.2 Thermodynamical and dynamical quantities derived from the measure- 135 ments

136 To describe the structure of the mesoscale eddies, surface maps of MADT anomaly<sup>1</sup> were computed at  
 137 the period and location of Phys-Indien measurements; from this anomaly, surface geostrophic velocities  
 138 ( $U, V$ ), relative vorticity and the Okubo Weiss quantity were obtained through derivations. The Okubo-  
 139 Weiss quantity is defined as the difference (in norm) between total deformation and relative vorticity

$$140 \quad OW = \sigma_{strain}^2 + \sigma_{shear}^2 - \omega^2$$

141 with the shear,

$$142 \quad \sigma_{shear} = \frac{\partial V}{\partial x} + \frac{\partial U}{\partial y}$$

143 the strain

$$144 \quad \sigma_{strain} = \frac{\partial U}{\partial x} - \frac{\partial V}{\partial y}$$

145 and the relative vorticity

$$146 \quad \omega = \frac{\partial V}{\partial x} - \frac{\partial U}{\partial y}$$

147 .  
 148 The Okubo-Weiss quantity is positive in regions where deformation dominates rotation, and it is negative  
 149 where vorticity dominates.

150 From the thermohaline data, density and spice (or spiciness) were calculated along the sections. In-  
 151 situ density was obtained by an equation of state from IOC and IAPSO (2010). Density anomaly  $\sigma_0$  is  
 152 displayed. Using  $T_0$ ,  $S_0$  and  $\rho_0$ , the reference temperature, salinity and density, of  $20^\circ\text{C}$ , 37 psu and 998  
 153  $\text{kg.m}^{-3}$ , spice  $\gamma$  is calculated via :

$$154 \quad \gamma = \gamma_0 [1 + \alpha (T - T_0) + \beta (S - S_0)].$$

155 (according to the definition by Smith and Ferrari (2009)). Spice concentrations highlight here the sub

---

<sup>1</sup>MADT anomaly is the residual of MADT minus an instantaneous spatial average, over the domain, of MADT

156 mesoscale structures at the periphery of the eddies. This variable shows a marked difference between  
 157 the salty waters trapped inside the mesoscale eddies and the fresher water patches surrounding them.  
 158 Using the slope of spice layers across isopycnic layers, their formation by the eddy shear and strain can  
 159 be studied.

160 Using velocities from the VM-ADCP measurements and density from the SeaSoar, a two-dimensional  
 161 Ertel potential vorticity (EPV, see Hoskins (1974)) can be calculated along each section

$$EPV = (f + \frac{\partial V_g}{\partial x}) \frac{\partial b}{\partial z} - \frac{\partial V_g}{\partial z} \frac{\partial b}{\partial x}$$

162 with  $b = -(\frac{g}{\rho_0})\rho$  the buoyancy. Its anomaly is

$$EPVA = EPV - f \frac{\partial \bar{b}}{\partial z}$$

163 Note that this calculation leads to small-scale some noise in the EPV anomaly due to the SeaSoar  
 164 and VM-ADCP resolution; the figures presented in the text are slightly smoothed for legibility.

### 165 **3 Onset of the Spring 2011 inter monsoon mesoscale situation**

166 The spring inter monsoon extends on average from February to May in the Arabian Sea. During this  
 167 period, the wind relaxes between the two local maxima of the winter and summer monsoon. In 2011,  
 168 the wind stress curl off Ra's Al Hadd changed sign from March to May. During this period, the wind  
 169 work leads to a deepening of the surface eddies(see L'Hégaret et al. (2015) and Vic et al. (2014)).

170  
 171 On figure 3, the MADT anomaly is displayed over the Sea of Oman and the northwestern Arabian  
 172 Sea from the winter monsoon to the beginning of the summer monsoon (November 2010 to June 2011).  
 173 In November 2010, an alongshore current, associated with a positive MADT anomaly, flowed along the  
 174 southern coast of Oman (the coastal "belt" of MADT anomaly described in L'Hégaret et al. (2015)); it  
 175 is driven by the Ekman currents. This current formed meanders in December 2010 and January 2011  
 176 along the coast of Oman. During these months, the mesoscale cyclone C1 exited the Sea of Oman and  
 177 the cyclone C2 propagated southwestward along the coast of Oman. Their surface temperature were  
 178 colder than that of the surrounding waters. Both the Owen fracture zone and the coastal current can  
 179 channel these cyclones along the coast.

180 From December 2010 through February 2011, the positive MADT anomaly in the Sea of Oman showed  
 181 the onset of a large anticyclonic eddy A1, having higher surface temperature than the cyclones. This  
 182 anticyclone A1 was part of a dipole recorded by ARGO floats, located nearly every spring near Ra's al  
 183 Hamra (see L'Hégaret et al. (2013)). South of Ra's Al Hadd, in the Arabian Sea, an alongshore meander  
 184 formed an anticyclone (A2), splitting apart the C1 and C2 cyclones. The first cyclone (C1) remained  
 185 east of Ra's Al Hadd until April; the second cyclone (C2) drifted southwestward, slowly warming up and  
 186 decreasing in intensity.

187 From March 2011 through May 2011, A1 splitted into two anticyclones, A1 and A3. Thus during the  
 188 Phys-Indien experiment three main vortices lined up along 61°E, south and north of Ra's Al Hadd: the  
 189 anticyclone at the mouth of the Sea of Oman (A3), the cyclone at Ra's al Hadd (C1) and the anticyclone  
 190 south of it (A2).

191 In May-June 2011, with the onset of the summer monsoon, the sea surface warmed up, cyclone  
 192 C1 weakens, A2 intensified in relation with the increasing negative wind stress curl and the alongshore  
 193 current started to form with a negative MADT anomaly in response to the onset of the summer monsoon.

194 The observed evolution of the structures in the region during the spring 2011 corresponds on average  
 195 to the usual spring inter monsoon, with large structures dominating the surface circulation and a strong  
 196 anticyclonic signature in the eastern Sea of Oman. The eddies influence the distribution of the sea  
 197 surface temperature, intensifying the thermal front near Ra's al Hadd (and later on, advecting cold  
 198 water offshore).

199 The following section will focus on the dynamical structure of these eddies and on their influence on the  
 200 water masses at depth, evidenced with the Phys-Indien experiment data.

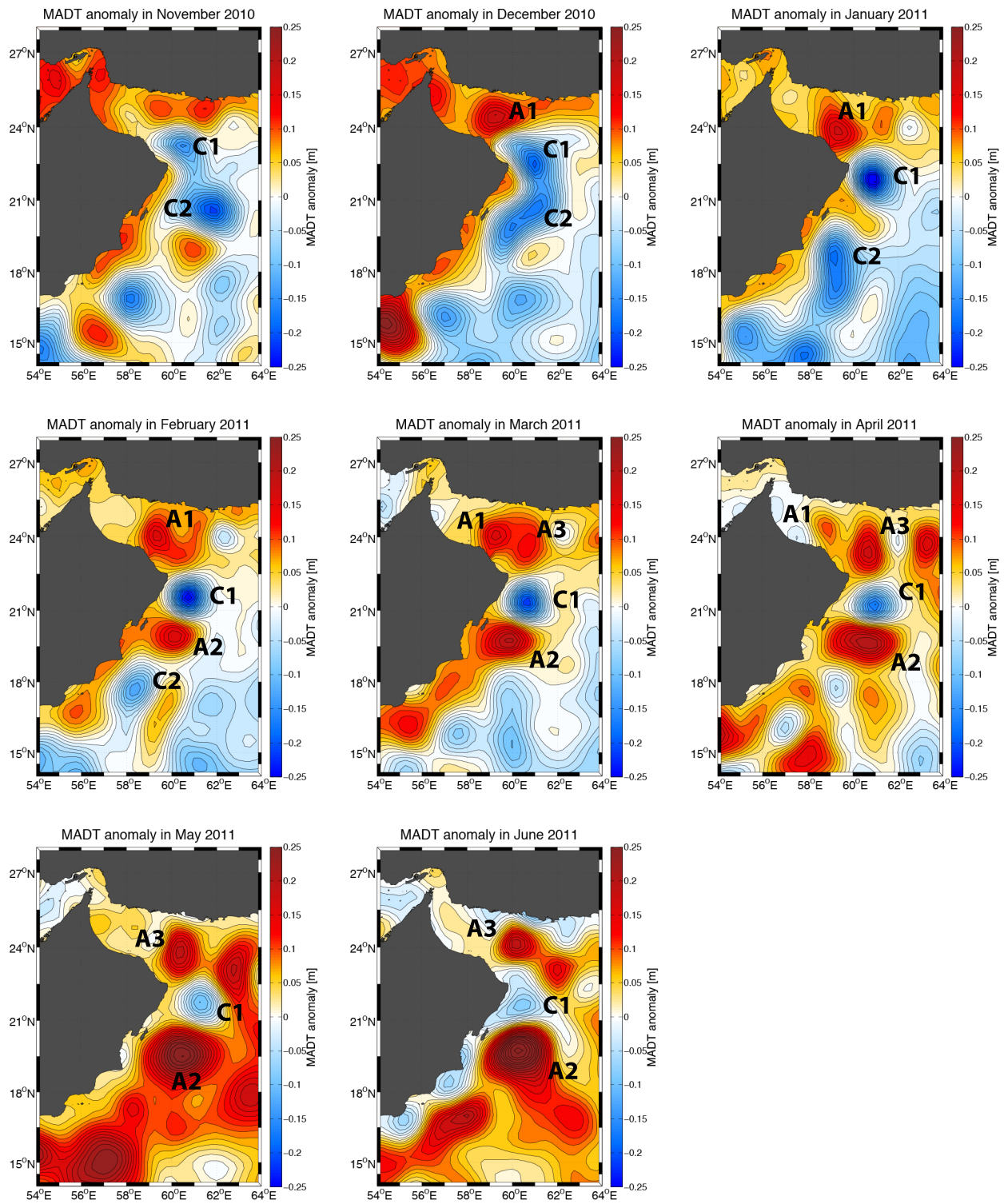


Figure 3: Maps of the MADT (altimetric) anomaly averaged over a month, from November 2010 to June 2011.

## 4 Structure of mesoscale eddies and their relation to the PGW distribution

This section focuses on the vertical characteristics of the eddies presented earlier and on their relations to the PGW outflow structure, using the Phys-Indien experiment data. In order to understand the relation between the vertical and horizontal structures, figure 4, displays surface fields derived from the MADT. The relative vorticity, Okubo-Weiss parameter and geostrophic velocities are calculated through derivations.

The relative vorticity field at the surface (upper right on figure 4), provides information on the horizontal extent and polarity of the eddies. The most intense features were A1 and C2 in the Arabian Sea with radii of 80 km. In the Sea of Oman, a train of eddies was found with alternating cyclones and anticyclones, with radii half the size of their Arabian Sea's counterparts, that is, about 40 km.

The Okubo Weiss parameter distribution at the surface shows that the structures are dominated by high concentrations of vorticity, and thus are robust when submitted to external strain or shear. C1 and A2 stood out as robust vortices on the bottom left panel 4, as well as A1. Furthermore, this Okubo Weiss parameter indicates the location where deformation dominates, that is, around C1, but also between A1 and the Omani coast, and north of A3 near the Iranian coast.

The bottom right panel of figure 4 displays the geostrophic velocity intensity and direction, at the surface. The most energetic currents were observed around C1, A2 and along the coastal "belt". In Bower and Furey (2012), Carton et al. (2012) and L'Hégaret et al. (2013), correlations were found between the surface circulation induced by the eddies and the structure of the salty outflows from the Red Sea and the Persian Gulf. The velocity map gives a first glimpse of the pathway of the PGW : in the western Sea of Oman, the water mass equilibrated and flowed along the southern coast, then it was ejected northward from the coast at Ra's Al Hamra, under the influence of A1, it flowed along the Iranian coast, eastward then southward (rotating around A1 and A3), and finally it recirculated around C1 before either escaping offshore in the Arabian Sea, or flowing southwestward around A2 and C2.

Superimposed on these maps, the positions of three sections of interest are indicated. A first section focuses on the Sea of Oman (SO section), a second one on the Arabian Sea (AS section) and a last one crosses a submesoscale lens of PGW off Ra's Al Hadd (lens section). These vertical sections present velocities measured with the VM-ADCP, the Ertel Potential Vorticity field, density and spice (see section 2 for computation).

### 4.1 Sea of Oman

From March 22<sup>nd</sup> to 30<sup>th</sup> the Phys-Indien experiment performed cross-sections in the Sea of Oman. A composite section (SO section) crossing this basin zonally, is presented and described here.

As observed in the surface maps (figure 4) of MADT anomaly and even more on surface velocity, the SO section crossed eddies with alternate polarities. The upper panel of figure 5 is a VM-ADCP velocity section showing an anticyclone between 56 and 57.8°E, a cyclone between 57.8 and 58.8°E and the A1 anticyclone from 58.8 and 60°E, the latter not sampled across its center. The density section of figure 5 is coherent with the eddy dynamical signatures, showing a lowering of the isopycnals below the anticyclones and a rising below the cyclone. The EPV anomaly field, though noisy, shows the structure of the eddies in the upper 100-150 m, but also a strong signature below 150 m depth.

The eddies are surface intensified in temperature and salinity anomalies, down to 200-300 m depth, but their dynamical influence reaches more deeply. Tilts of the velocity field are found below the central cyclone at 58°E and also at 57.5°E. These tilts are colocalized with a spreading of the isopycnals, indicated by grey and green crosses on the density panel figure 5. The spice section (see below) will identify the structures associated with these tilts.

The spice section (bottom panel figure 5) is an efficient marker of the PGW structure. The first noticeable feature at 100 m depth is the strong gradient of spice across 58.8°E (the blue line), at the western edge of anticyclone A1. West of this line, several patches of PGW are marked by high spice concentrations, with two lenses at 58°E and at 57.5°E (green and grey lines); east of 58.8°E, no such patch is observed. These lenses are correlated in position with negative anomalies on the EPV anomaly field. The circulation at the PGW depth from 58 to 59°E was northward with a recirculation around A1 and A3; this corresponds to the ejection of PGW from the Omani coast near Ra's Al Hamra. Below

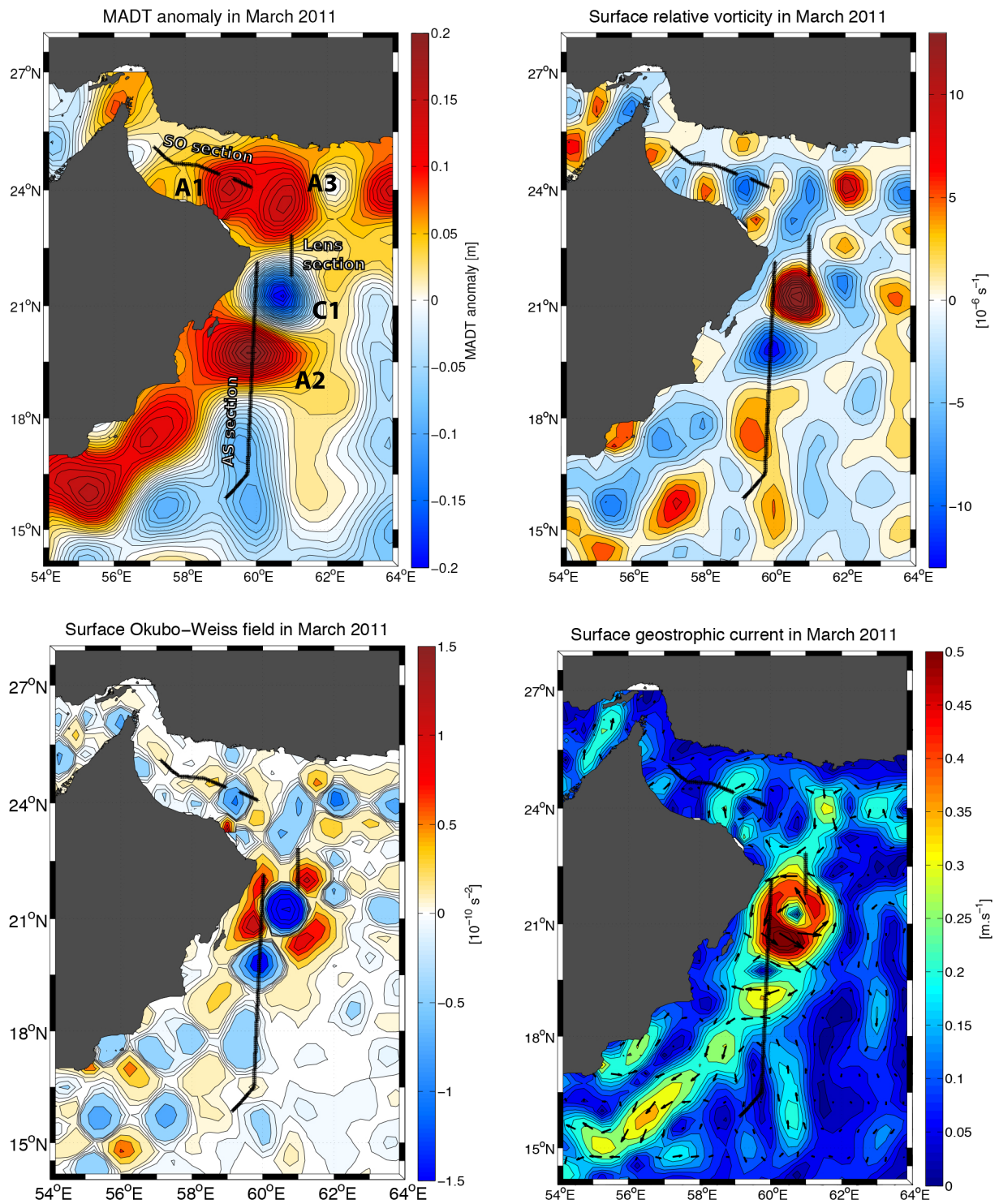


Figure 4: Maps of the surface fields averaged from 16 to 30 March 2011, during the measurements south of Ra's Al Hadd (AS section), in the lens off Ra's Al Hadd (lens section), and across the Sea of Oman (SO section). Fields are : ADT anomaly (top, left); relative vorticity (top, right); Okubo-Weiss criterion (bottom, left); geostrophic velocity (bottom, right).

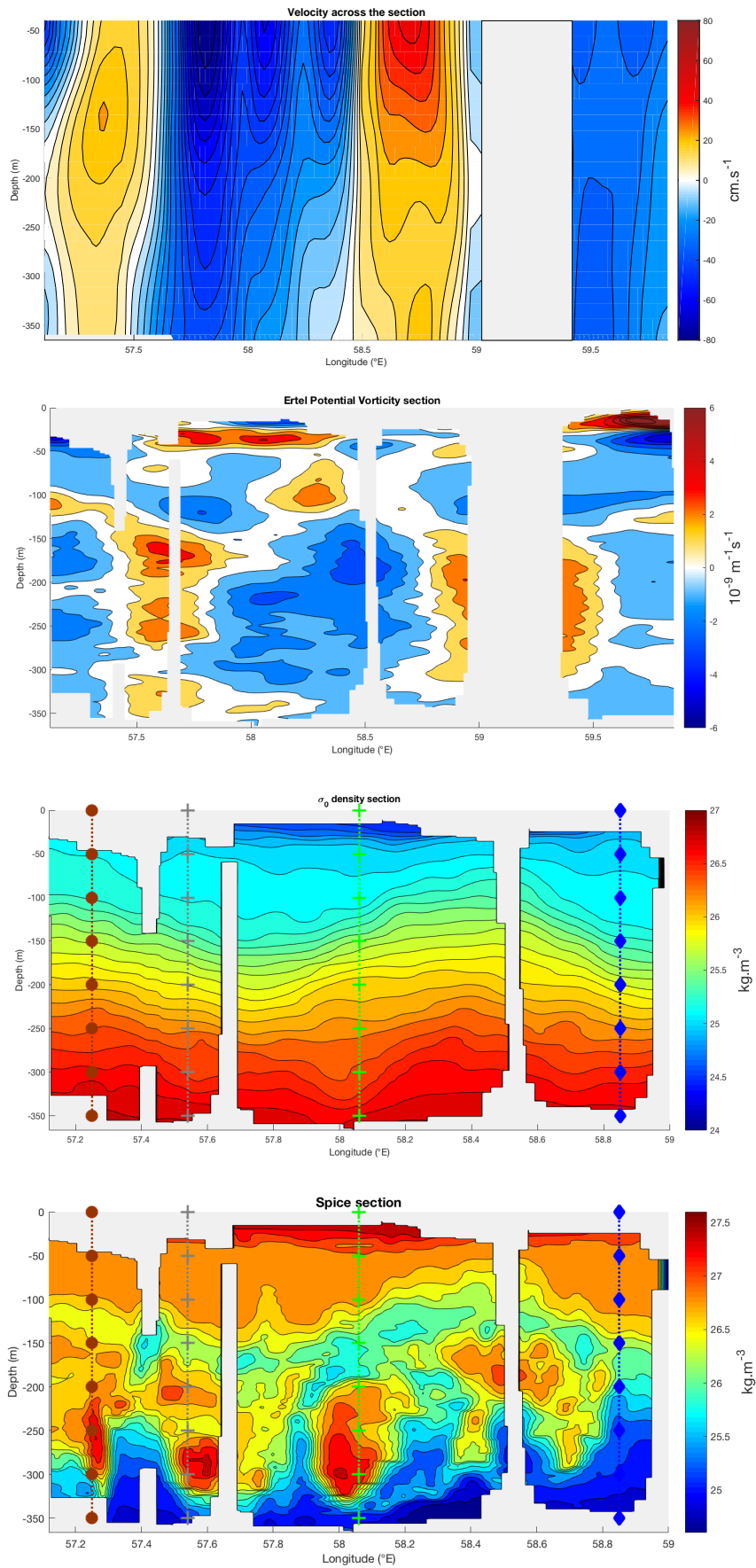


Figure 5: SO sections of the eddies, south of Ra's Al Hadd from surface down to 350 m depth. Measurements and derived quantities are : VM-ADCP velocities, positive towards the north; the Ertel Potential Vorticity anomaly is derived from VM-ADCP and SeaSoar fields;  $\sigma_0$  potential density and spice.

Month	January	February	March	April	May	June
Density ( $\text{kg.m}^{-3}$ )	26.62	26.61	26.82	26.95	26.92	26.32
Salinity (psu)	38.46	38.26	38.29	38.48	38.50	37.89
Temperature ( $^{\circ}\text{C}$ )	22.79	22.31	21.66	21.70	21.87	22.33
Month	July	August	September	October	November	December
Density ( $\text{kg.m}^{-3}$ )	25.91	26.01	26.25	26.01	25.74	26.34
Salinity (psu)	37.53	37.63	37.83	37.66	37.32	38.29
Temperature ( $^{\circ}\text{C}$ )	22.80	22.74	22.42	22.78	22.84	23.32

Table 1: Maximal PGW density, and associated salinity and temperature, before cascading in the Sea of Oman for each month extracted from the GDEM climatology.

253 the surface, this section also shows filaments of IOCW (with weaker spice), wrapping around the PGW  
254 patches.

## 255 4.2 Arabian Sea

256 The Arabian Sea (AS) section studied here is located south of Ra's Al Hadd, from  $16^{\circ}\text{N}$  to  $22^{\circ}\text{N}$  almost  
257 along  $60^{\circ}\text{E}$ ; it was carried out from March  $16^{\text{th}}$  to  $19^{\text{th}}$  2011.

258 The surface fields from figure 4 indicated that the AS section crossed, from south to North, cyclone  
259 C2, the core of anticyclone A1 and the western edge of cyclone C1; thus, between  $19^{\circ}\text{N}$  and  $20.5^{\circ}\text{N}$  was  
260 a region dominated by vorticity concentrations, and north of  $20.5^{\circ}\text{N}$  by deformation. Both the velocity  
261 horizontal map and vertical section show the intensity of the A2 and C1, with currents above  $80 \text{ cm. s}^{-1}$   
262 (upper panel figure 6). Furthermore, they indicate that the eddy velocities remained noticeable below  
263  $600 \text{ m}$  depth, with values above  $10 \text{ cm.s}^{-1}$  (not shown). The density section exhibits intense lowering  
264 and rising of the isopycnals, below C1 and A2. In the EPV anomaly section, anticyclone A2 is clearly  
265 identified, with a negative core between  $50$  and  $150 \text{ m}$  depth.

266 The spice section (bottom panel of figure 6) displays less turbulence than that in the Sea of Oman;  
267 nevertheless a few structures are of interest. Below the surface, isopycnal spacing is observed at  $18.8^{\circ}\text{N}$   
268 at  $160 \text{ m}$  depth (yellow line), related to a spicier structure, characteristic of a PGW lens, with a diameter  
269 of  $40 \text{ km}$ . As well, less spicy water wrapped and flowed upward along the eddies, as noted at  $19.4^{\circ}\text{N}$   
270 (cyan line). The PGW containing eddies stirred and advected upward IOCW.

271 In the Sea of Oman, the outflowing PGW is subject to strong mixing, and is fragmented, with  
272 detached lenses at depth, and more isolated patches above. In the Arabian Sea, the eddies can advect  
273 PGW in their core. Water masses at their rim undergoes a strong deformation. The following sections  
274 focuses on PGW recording during the experiment, its pathway, structure and evolution.

## 275 5 PGW characteristics, pathway and submesoscale structures

276 Table 1 indicates the peak thermohaline values of the PGW (from climatology), as it flows out of the  
277 Strait of Hormuz. The highest densities (above  $26.6 \text{ kg.m}^{-3}$ ) are found from January to to May, with a  
278 salinity well above  $38 \text{ psu}$ . This density decreases below  $26 \text{ kg.m}^{-3}$  in late summer (July-August) and  
279 early winter (October-November) as the outflow becomes fresher. The value of the PGW density is thus  
280 highly seasonal.

### 281 5.1 Sea of Oman

282 The upper panels from figure 7 presents the thermohaline characteristics at different locations. All the  
283 profiles indicate salinity above  $37.8 \text{ psu}$ , except for the profile at the western edge of A1 (blue crosses).  
284 All of them peak in salinity at  $\sigma_0 = 26.3\text{-}26.4 \text{ kg.m}^{-3}$ , characteristic of PGW. A second peak in salinity  
285 is found at  $\sigma_0 = 25.8 \text{ kg.m}^{-3}$ , rarely above  $37 \text{ psu}$ ; it can be observed on the grey profile (located on the  
286 spice section; bottom panel of figure 5). This more dilute PGW, is well marked on the blue profile; it  
287 a priori originated from the outflow during a previous season, and must had recirculated in the western  
288 end of the Sea of Oman, as observed in a numerical simulation (L'Hégaret et al. (2015)).

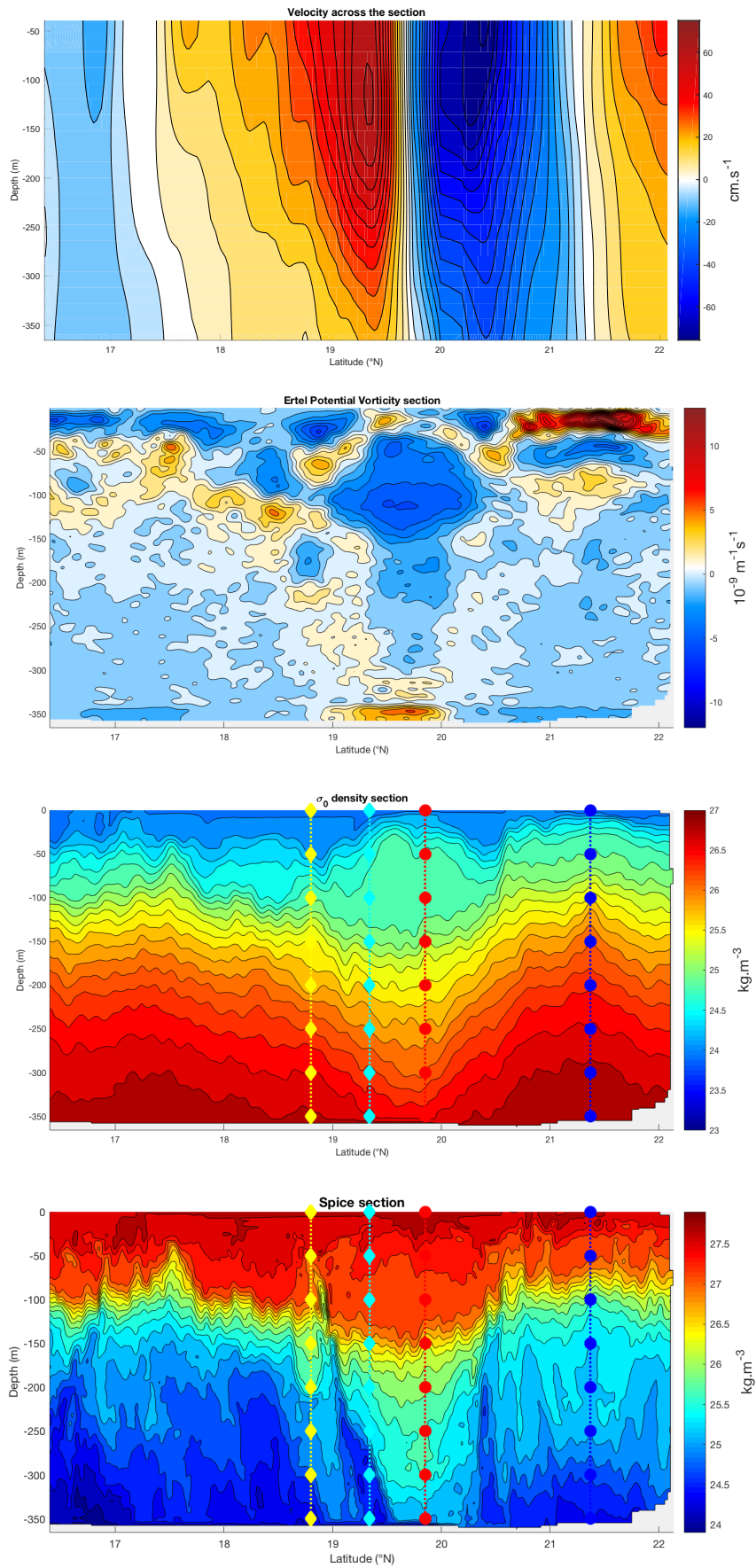


Figure 6: AS sections of the eddies, south of Ra's Al Hadd from surface down to 350 m depth. Measurements and derived quantities are : VM-ADCP velocities, positive towards the north; the Ertel Potential Vorticity anomaly is derived from VM-ADCP and SeaSoar fields;  $\sigma_0$  potential density and spice.

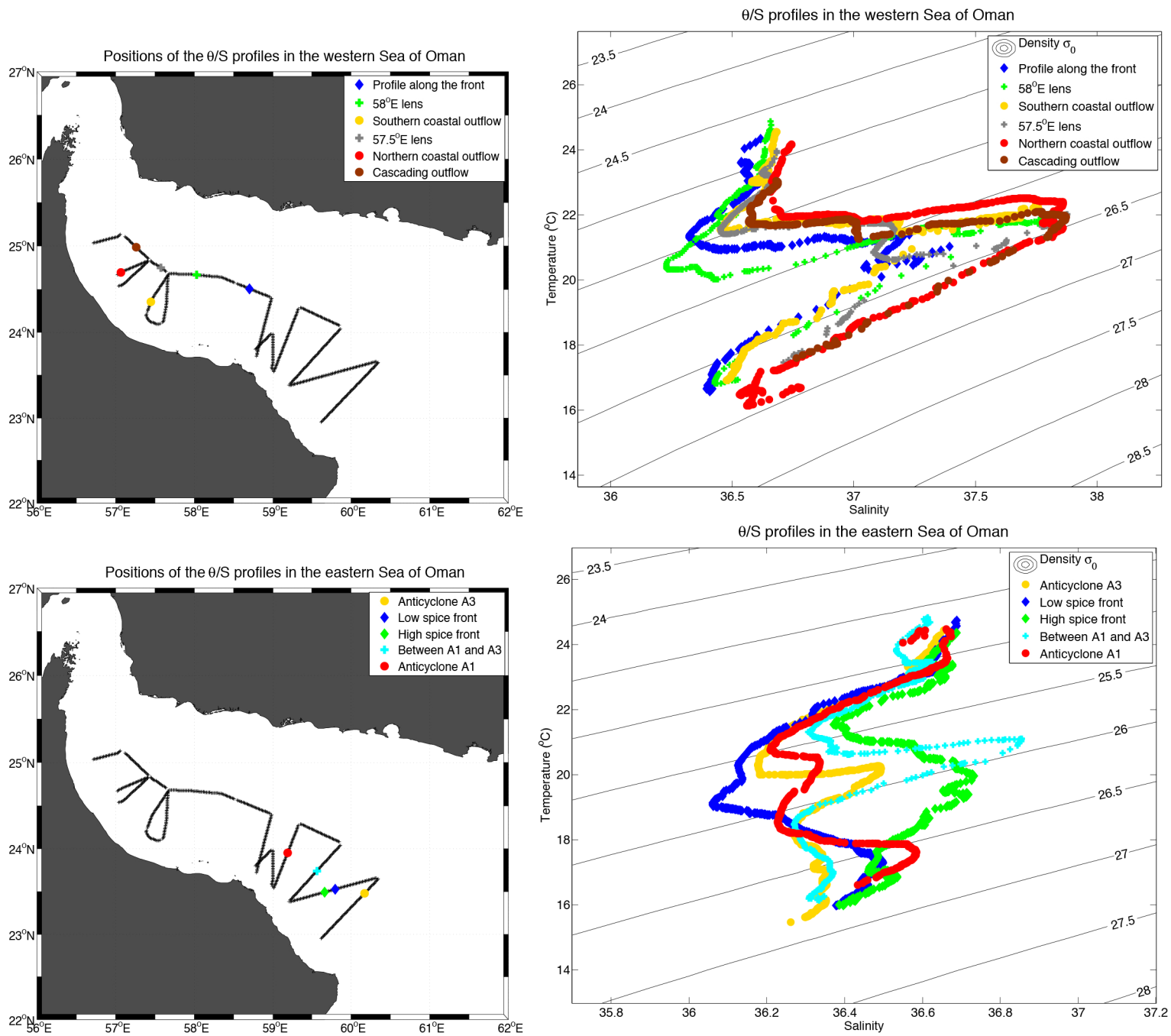


Figure 7: Potential temperature over salinity profiles (right) and their locations of interest (left); in the western Sea of Oman (up) and eastern Sea of Oman (down). Top panel :

- Blue diamond : Profile out of the salty outflow;
- Green cross : 58°E lens;
- Yellow circle : southern profile in the PGW outflow along the coastal slope;
- Grey/Black cross : 57.5°E lens;
- Red circle : northern profile in the PGW outflow along the coastal slope;
- Brown circle : cascading PGW outflow.

Bottom panel :

- Yellow circle : profile inside the anticyclone A3;
- Blue diamond : Low spice profile, observed in the periphery of A3;
- Green diamond : High spice profile, observed in the periphery of A3;
- Cyan cross : at the periphery of the anticyclones A1 and A3;
- Red circle : profile inside the anticyclone A1.

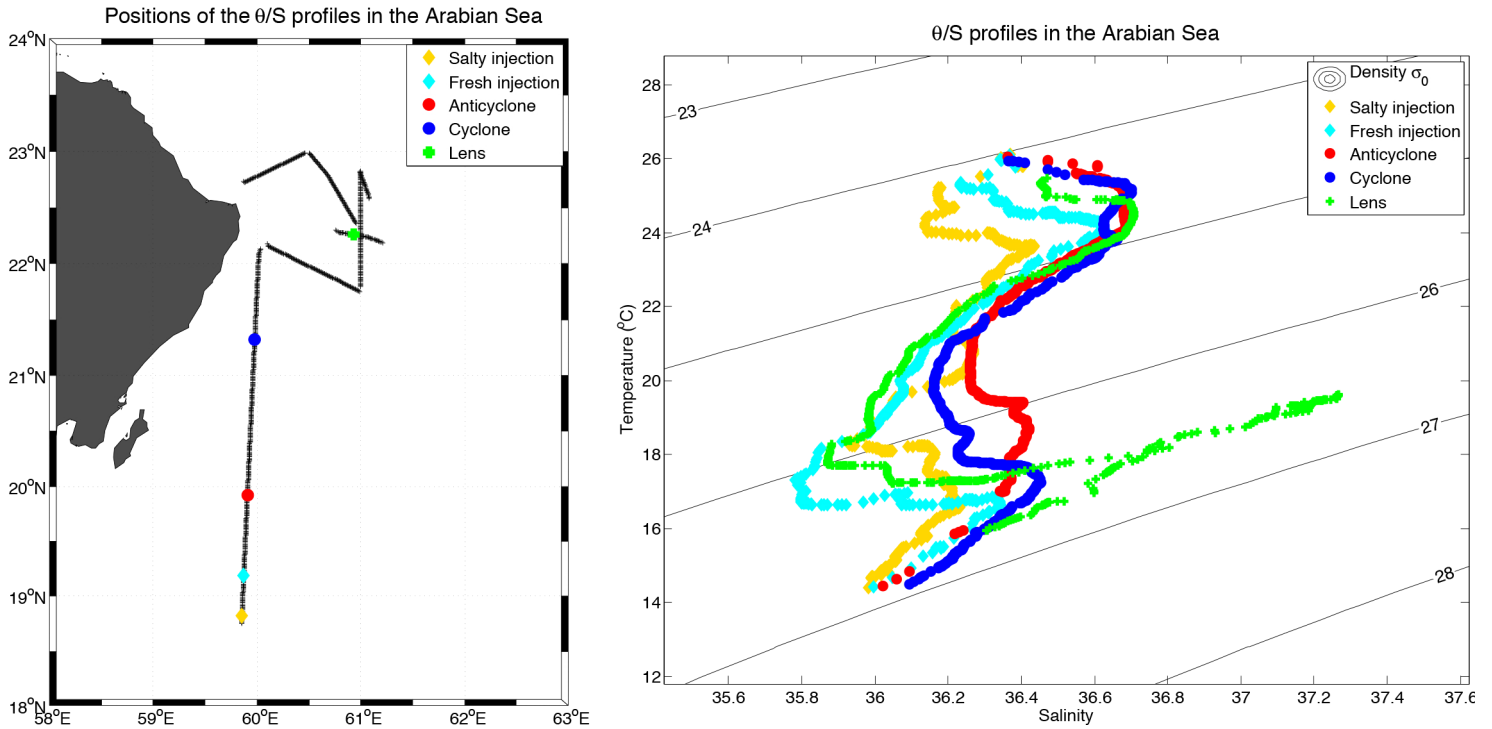


Figure 8: Potential temperature over salinity profiles (right) in the western Arabian Sea at various locations of interest (left). From north to south :

- Yellow diamond : Salty injection around anticyclone A2;
- Cyan diamond : Fresh injection around anticyclone A2;
- Red circle : inside anticyclone A2;
- Blue circle : inside cyclone C1;
- Green cross, at the periphery of the anticyclone;
- Red circle : inside the lens off Ra's Al Hadd.

289 The coastal outflow of PGW appears on the brown and red profiles (upper panels of figure 7). They  
 290 display wide peaks at  $\sigma_0 = 26.3\text{-}26.4 \text{ kg.m}^{-3}$  at 37.9 psu. To the south, a thinner salinity peak corresponds  
 291 to PGW mixing with IOCW; a peak of lighter PGW is observed at  $\sigma_0 = 25.8 \text{ kg.m}^{-3}$  with salinity at  
 292 37.2 psu. Both profiles across the PGW lenses peak in salinity at  $\sigma_0 = 26.4 \text{ kg.m}^{-3}$ , as the core of these  
 293 structures is preserved from dilution.

294 Above the lens at  $57.5^\circ\text{E}$ , a patch of PGW at  $\sigma_0 = 25.8 \text{ kg.m}^{-3}$  with salinity of 37.2 psu is found.  
 295 The lens at  $57.5^\circ\text{E}$  (grey profile) had a diameter of 15 km, a height of 50 m, advecting diluted PGW  
 296 above it, while the lens at  $58^\circ\text{E}$  (green profile) had a diameter of 25 km and a height of 100 m. The first  
 297 one must have formed earlier, probably in early winter, recirculating and slowly eroding in the western  
 298 Sea of Oman, whereas the second must have formed later.

299 The bottom panels of figure 7 present thermohaline profiles in the eastern Sea of Oman.  
 300 The red and yellow profiles show the different characteristics of the PGW trapped in anticyclones A1 and  
 301 A3. Anticyclone A3 was formed between February and March 2011 and had only one extremum of PGW  
 302 salinity at  $\sigma_0 = 25.8 \text{ kg.m}^{-3}$  (see figure 3). Anticyclone A1 formed in December 2010, and enclosed two  
 303 PGW maxima (see red profile): the first maximum corresponds to denser waters than those recorded in  
 304 the western Sea of Oman, below  $\sigma_0 = 26.6 \text{ kg.m}^{-3}$ ; the second maximum was more diluted, at  $\sigma_0 = 25.6$   
 305  $\text{kg.m}^{-3}$ , and was lighter than that observed in A3. Thus during its formation, anticyclone A1 enclosed  
 306 two PGW patches from different seasons.

## 307 5.2 Arabian Sea

308 Figure 8 presents thermohaline profiles in the Arabian Sea. Cyclone C1 (blue profile) formed at the same  
 309 period as anticyclone A1, in December 2010 or early January 2011 (see figure 3). Similarly, it shows a

310 peak of PGW at  $\sigma_0 = 26.6 \text{ kg.m}^{-3}$ , slightly more diluted, 0.2 psu below A1 as it lies downstream.

311 Anticyclone A2 (red profile in figure 8) formed one month later, between January and February 2011.  
312 Inside it, the PGW peak was less marked and wider: this water mass mixed with the surrounding IOCW.  
313 The density ranged from 26 to  $26.3 \text{ kg.m}^{-3}$ , indicating a PGW flowing out of the Persian Gulf from  
314 January to May 2010.

315 The cyan and yellow profiles in figure 8 focus on the layers wrapping around anticyclone A2, and  
316 located at its southern edge.

317 The cyan profile indicates that IOCW, with salinity below 35.8 psu, in the density range of the PGW,  
318 was advected upward at the eddy rim. The yellow profile crossed PGW just below the thermocline  
319 (see density density section, figure 6); the salinity peak is found at  $25.5 \text{ kg.m}^{-3}$ . This light PGW is  
320 comparable to that observed in the core of A3 (see bottom panel figure 7, yellow profile) but with a  
321 weaker salinity; thus it formed farther from the Sea of Oman. This PGW was advected around A2, also  
322 with an upward motion.

### 323 5.3 Submesoscale lens off Ra's Al Hadd

324 The lens section displayed on figure 4 corresponds to the measurements achieved between the 19<sup>th</sup> and  
325 the 20<sup>th</sup> March 2011. This section extended between anticyclone A3 and cyclone C1 and recorded  
326 a submesoscale lens of PGW. The surface fields indicates westward geostrophic velocities, above  $0.4$   
327  $\text{m.s}^{-1}$ , in a region dominated by deformation.

328 The velocity section (figure 9, top) shows the westward velocities from the surface down to 200 m  
329 depth, intensifying up to  $0.8 \text{ m.s}^{-1}$  near cyclone C1. Between  $22.1^\circ\text{N}$  and  $22.4^\circ\text{N}$ , and 250 and 400 m  
330 depth, an anticyclonic motion is observed on the zonal velocity section with speed of about  $0.2 \text{ cm.s}^{-1}$ ;  
331 but this signal is strongly dominated by the velocity of the surface eddy. This anticyclonic structure also  
332 appears on the EPV anomaly field figure 9 by the negative core around 300 m depth and by the spacing  
333 of the isopycnals.

334 The spice section (bottom panel of figure 9) confirms the presence of a lens shaped structure between  
335 250 and 350 m depth, with a diameter of 25 km, and the green profile of figure 8 crossing the center of  
336 the lens, indicates a temperature of  $19^\circ\text{C}$  and salinity above 37.3 psu at its center; the density is  $\sigma_0 =$   
337  $26.6 \text{ kg.m}^{-3}$ .

338 On a perpendicular cross section (not presented here), the lens has a diameter of 33 km; this shows  
339 that this lens was elliptical, as confirmed by a third section. The total salt and heat content, inside the  
340  $36.6 \text{ psu}$  (or  $18^\circ\text{C}$ ) contour, is  $2.59 \cdot 10^{12} \text{ kg}$  and  $6.54 \cdot 10^{19} \text{ J}$ , and the lens volumic transport (across the  
341 section) is above  $0.4 \text{ Sv}$ . The spice section also displays a layer of IOCW above the lens at  $22.1^\circ\text{N}$ .

342 The peak salinity above 37.3 psu is observed only in the Sea of Oman at this period; this density  
343 corresponds to a PGW which flowed out of the Strait of Hormuz in early 2011; therefore this lens likely  
344 formed in the Sea of Oman.

345 In L'Hégaret et al. (2015), several mechanisms leading to the formation of eddies containing PGW were  
346 listed. Here, two possible mechanisms are assessed.

347 In winter, lee eddies form downstream of Ra's Al Hamra; these eddies retain high salinity water in  
348 their core before eroding for three months. This mechanism was observed in a high resolution HYCOM  
349 simulation, where lee eddies were the only structures retaining salinity above 37 psu in the Arabian Sea  
350 and possessing a strong altimetric signature. In the MADT anomaly maps between January and March  
351 2011, no such signature was observed; this renders this mechanisms rather unlikely here.

352 The other mechanism for the formation of this lens in the Sea of Oman would be the ejection of  
353 PGW fragments from the coastal outflow, under the action of mesoscale eddies. This can occur near  
354 Ra's al Hamra in late winter, early spring or south of Ra's Al Hadd. In the Sea of Oman, the maximal  
355 deformation affecting the PGW outflow occurred near Ra's Al Hamra. This mechanism implies that the  
356 PGW lens would have drifted about 600 km, around anticyclone A2. The anticyclone velocity was at  
357 least  $0.4 \text{ m.s}^{-1}$  at the depth of the outflow; therefore, the lens would have taken 15 days to travel this  
358 distance; this would lead to a lens formation in early March, coherent with the PGW density in the core  
359 of the lens. Another possible formation site is south of Ra's Al Hadd. Cyclone C1 would have ejected the  
360 lens and advected it. With a velocity of about  $0.6 \text{ m.s}^{-1}$ , it would have taken 10 days between ejection  
361 and the Phys-Indien measurements. Nevertheless, the salinity and density of the lens were higher than  
362 those of the PGW outflow near Ra's Al Hadd. Therefore, lens formation near Ra's al Hamra was more  
363 likely.

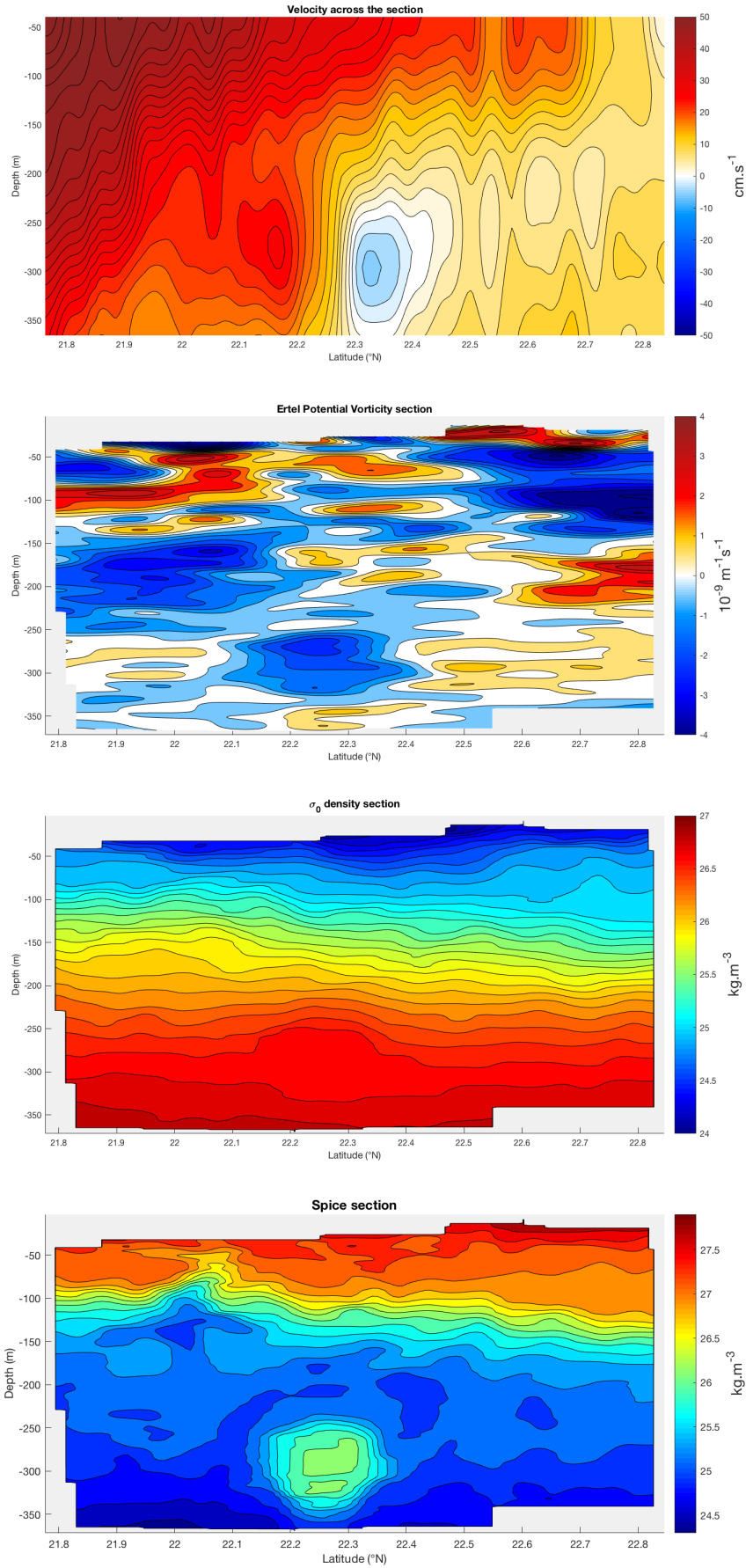


Figure 9: Sections across the lens off Ra's Al Haddad from the surface down to 350 m depth. Measurements and derived quantities are : VM-ADCP velocities, positive towards the north; the Ertel Potential Vorticity anomaly is derived from VM-ADCP and SeaSoar fields;  $\sigma_0$  potential density and spice.

364 During the Phys-Indien 2011 experiment, two deep drogued surdrift floats and three ARGO floats  
 365 were seeded in this submesoscale lens. The surdrift floats allow a hourly tracking of the lens, and the  
 366 ARGO floats record temperature and salinity with a surfacing every 5 days. All these floats followed a  
 367 northwestward trajectory for the first 4 days of measurements. After this period, the three ARGO floats  
 368 were ejected, as revealed by their recorded salinity; so were the surdrifts which then followed anticyclone  
 369 A3, north of Ra's Al Hadd. One surdrift buoy lost its drogue and performed inertial loops. This inability  
 370 to track the lens for long durations underlines the strong deformation that it was subjected to.

371 The deformation of a lens by external shear or strain was studied by Ruddick (1987): as strain  
 372 increases, the lens becomes more elliptical and unsteady, before either breaking up or readjusting. And  
 373 indeed, this submesoscale lens off Ra's Al Hadd, was elliptical and embedded in a strong deformation  
 374 field due to the strong mesoscale eddies in its vicinity. Walsh (1995) studied the deformation of a lens in  
 375 an uniform large scale shear in a model. With  $q$  the potential vorticity of the lens,  $S$  the external shear,  
 376  $a$  and  $b$  the long and short axis of the ellipse, the theoretical lateral deformation of the eddy is :

$$\frac{a-b}{a+b} = \frac{15 S}{8 q}$$

377 With  $a = 33$  km and  $b = 20$  km,  $S = 0.1q$ . The potential vorticity of the lens was about  $8 \cdot 10^{-5} \text{ s}^{-1}$ ,  
 378 leading to  $S \sim 10^{-5} \text{ s}^{-1}$ . At the depth of the lens, the mesoscale eddies velocities and radius gave a  
 379 measured shear of  $\frac{\partial V}{\partial r} \sim \frac{V}{R} \sim \frac{0.5}{50 \cdot 10^3} \sim 10^{-3} \text{ s}^{-1}$ , the same magnitude as calculated with the Walsh  
 380 (1995) model.

#### 381 5.4 Recurrence of PGW lenses

382 Numerous ARGO floats (with WHOI numbers 2901370, 2901387, displayed on figure 10 or WHOI num-  
 383 bers 1901187, 1901202 and 6900902) sampled PGW in the Sea of Oman. Until the early summer monsoon,  
 384 localized patches of PGW with salinity above 37.2 psu, temperature around 20°C and  $\sigma_0 \approx 26.5 \text{ kg.m}^{-3}$   
 385 are observed, with a spacing of the isopycnals above and below them. These patches are found either off  
 386 Ra's Al Hadd or off the Sea of Oman.

387 In June 2011, anticyclone A3 was advected northward as the summer monsoon began, thus reducing  
 388 the deformation field off Ra's Al Hamra. To break the PGW outflow into lenses and filaments, Vic et al.  
 389 (2015), using a high resolution numerical model, showed that a strong shear and strain is necessary. Thus  
 390 fewer submesoscale PGW structures are expected to be observed during the summer monsoon (when  
 391 the deformation field is less intense); but due to a lack of regular observations at the depth of PGW.  
 392 Note that another possible mechanism for PGW outflow breaking is baroclinic instability which depends  
 393 on the vertical shear of velocity. This speed should also be recorded regularly on the continental slope  
 394 near Ra's al Hamra. Baroclinic instability has been mentioned by Pous et al. (2004) to explain fragment  
 395 detachment from the outflow in fall 1999 (during the GOGP1999 experiment).

#### 396 5.5 Synthetic view of the PGW pathway and characteristics

397 Maps of Eulerian transport (figure 11) are computed to follow the pathways of the PGW outflow. The  
 398 Eulerian transport directions can be related to the in-situ velocity sections and to the altimetric maps  
 399 (surface currents), already presented. Indeed, in the Sea of Oman, the volumic transport was anticyclonic  
 400 with two cells, between 57 and 58.5°E, and between 58.5 and 60°E. This corresponded to A1 and A3.  
 401 In the Arabian Sea, the strong jet between C1 and A2 led to the eastward 6.4 Sv transport at 20.5°N,  
 402 while an opposite westward jet between A2 and C2 at 18°N transported 2.8 Sv.

403 Figure 12 indicates that, in the Sea of Oman, the front already seen in the SO section appeared  
 404 with warm and salty PGW west of 59°E, and fresher waters with patches of higher salinity east of 59°E.  
 405 This front, due to the strong anticyclone A1 and a cyclone west of it, halted the zonal spreading of the  
 406 PGW and advected it northward. The penetrating IOCW was also blocked from the east by the front,  
 407 as observed on the recording of an ARGO float (number 2901370) in March 2011 (see figure 10).

408 In the western Sea of Oman, newly outflowing PGW cascaded down the southern continental slope,  
 409 where the saltiest PGW was observed. In late March, the anticyclonic circulation of the basin drove the  
 410 water westwards (see transport figure 11, top). This motion was observed on an ARGO float (number  
 411 2901387, see figure 10), looping cyclonically from March to May, then moving northwestward, towards

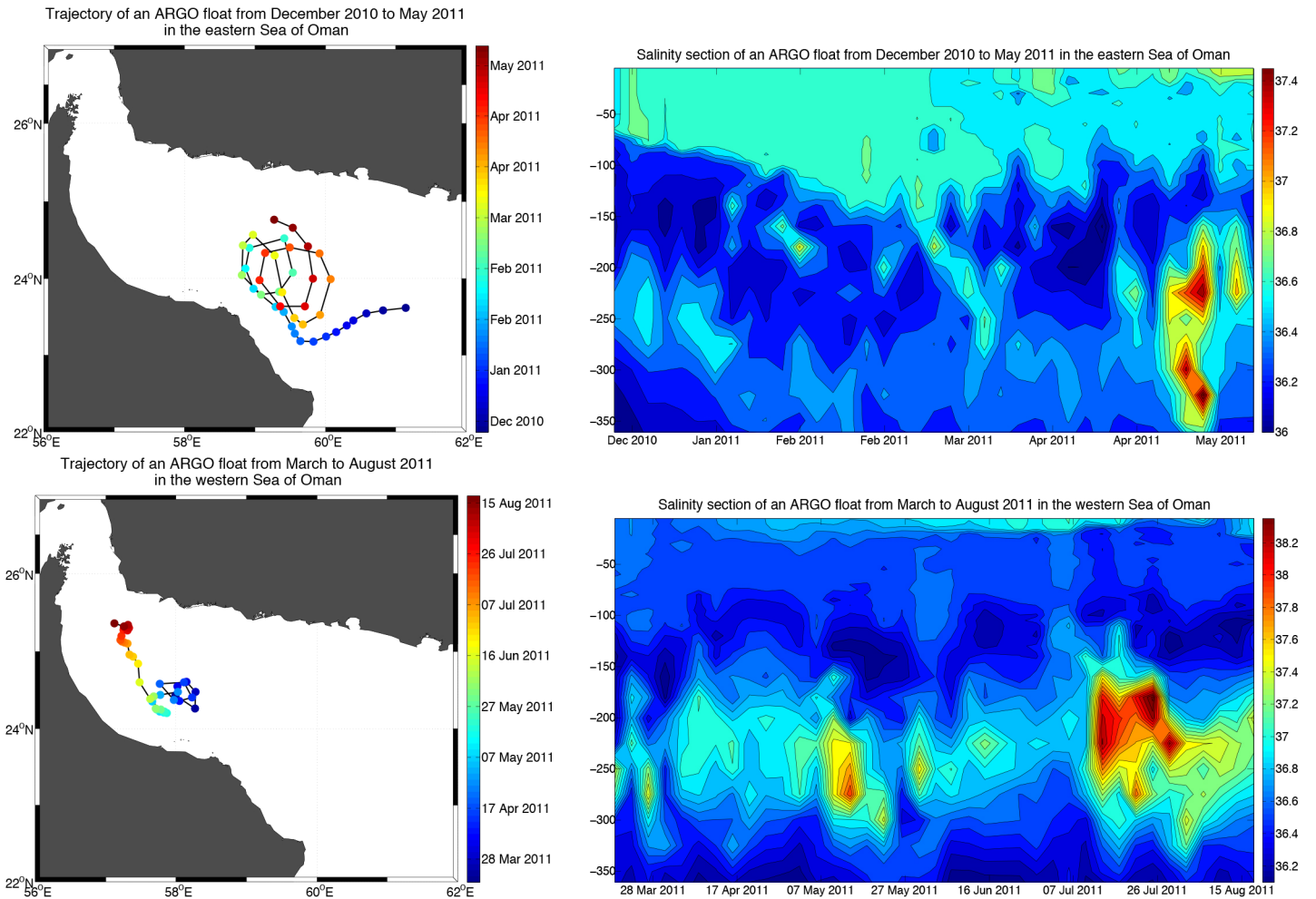


Figure 10: ARGO floats 2901370 (top) and 2901387 (bottom), trajectories (left) and salinity section (right) in the eastern and western Sea of Oman. Float 2901370 (up) enters the Sea of Oman with anticyclonic loops, is stopped by the front in March 2011 and then looped cyclonically until late May 2011, between A1 and A3. Float 2901387 looped cyclonically from March to May 2011 before moving northwest. Patches of salty PGW are observed, with the strongest in July when the float is found near the position of cascading PGW.

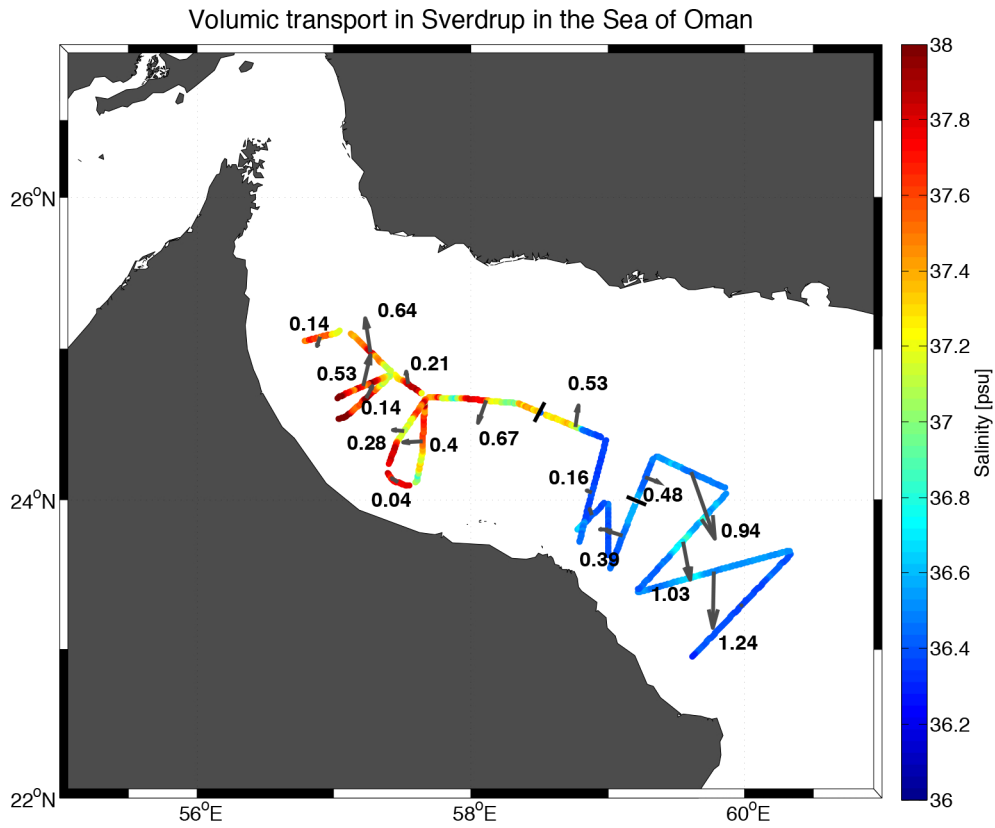


Figure 11: Eulerian volumic transport across the SeaSoar/VM-ADCP sections in the Sea of Oman (top) and in the Arabian Sea (bottom). Arrows indicates the direction, the values are in Sverdrup and in color is indicated the maximum of salt in the PGW layer.

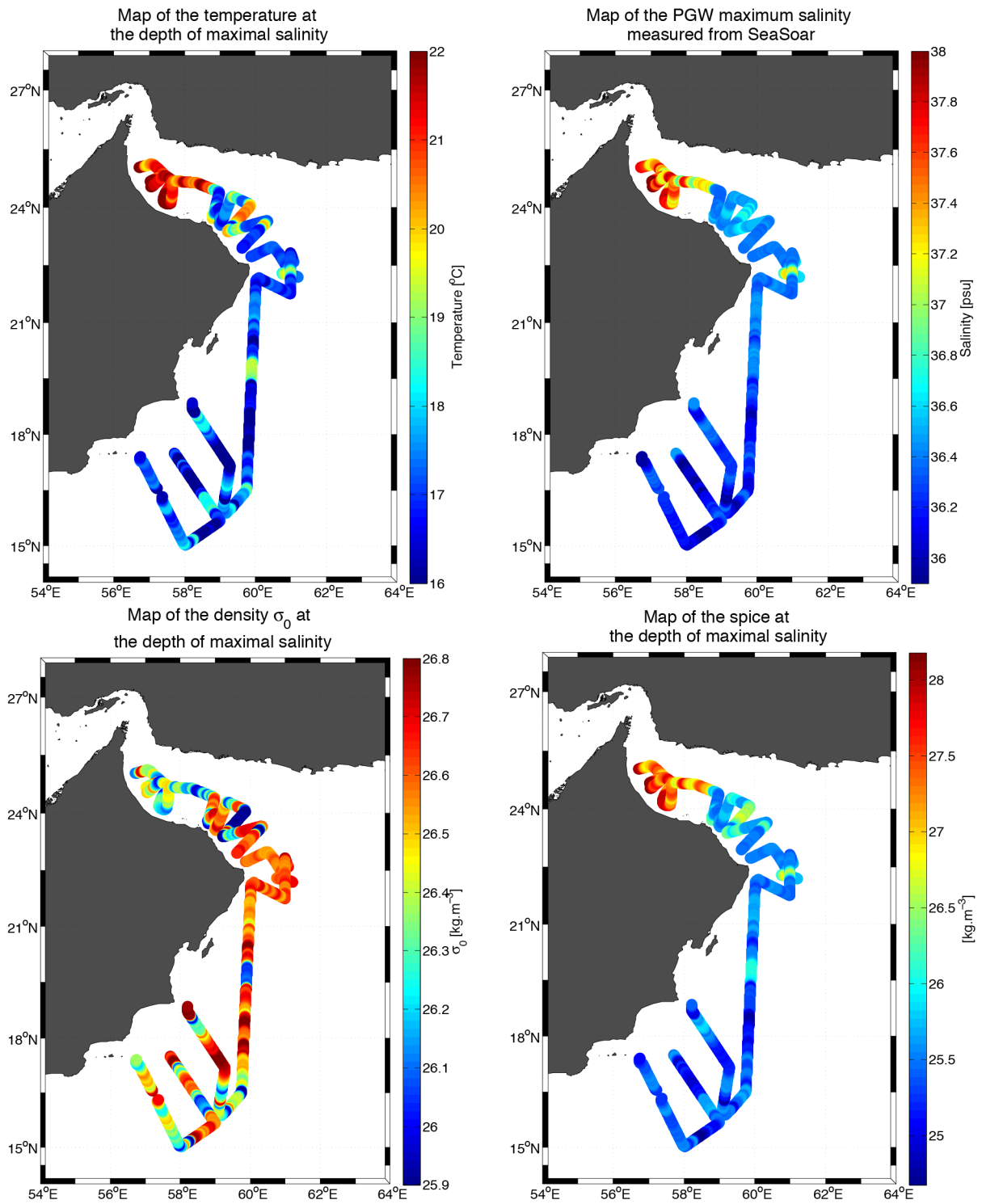


Figure 12: Maximal thermohaline characteristics of the Persian Gulf Water (from the SeaSoar measurements, for  $\sigma_0$  between 26 and 26.7). The variables are : temperature (top, left); salinity (top, right);  $\sigma_0$  at the maximal salinity depth (bottom, left); and spice at the same depth (bottom, right).

412 the Strait. This recirculation, associated with that induced by A1, forced PGW to remain in the western  
 413 part of the basin; therefore, PGW from two different seasons, was present in the same region. This was  
 414 confirmed by the map of the PGW density (bottom, left panel of figure 12) with various values in the  
 415 western basin. This was also noticed on the blue and green profiles of figure 7 where two neighbouring  
 416 samples have different characteristics.

417 Furthermore, fragmented PGW was found at the periphery of A1 and A3 (see bottom panel of figure  
 418 7, cyan profile); this peripheral PGW had high salinity, but it was more diluted in the core of these  
 419 eddies; figure 7 (bottom, red profile) showed a difference of about 0.8 psu between the periphery and  
 420 the core; this might be due to the intrusion mechanism of PGW into the core, or to earlier mixing with  
 421 fresher, colder IOCW. The recent, denser PGW from winter, was mainly observed in A1, whereas older,  
 422 mixed and lighter PGW, is found in A3.

423 In March 2011, the PGW mainly exited the Sea of Oman along its northern boundary, circling around  
 424 anticyclones, but small patches below 36.8 psu were observed, confined to the southern coast between  
 425 Ra's Al Hamra and Ra's Al Hadd (see green profile in the bottom panel of figure 7). The PGW density  
 426 there, ranged from 25.6 to 26.3 kg.m<sup>-3</sup>; this indicates mixed PGW from different seasons with IOCW  
 427 trapped between A1, A3 and the coast; indeed, this small region dynamics was dominated by deformation  
 428 (bottom left panel of figure 3, south-east of Ra's Al Hamra).

429 In the Arabian Sea, the PGW evolution around eddies C1 and A2 was similar to that in the Sea of  
 430 Oman, but with stronger dilution, by more than 1 psu (see figure 8). In anticyclone A2, the PGW layer  
 431 was warmer (top left panel of figure 12), with temperature above 19.5°C; this was a priori due to heat  
 432 transfer from the ASHSW layer in this intense eddy. South of 18°N, the PGW was strongly diluted and  
 433 mixed with the IOCW.

434 Both in the Arabian Sea and in the Sea of Oman, layers of colder and fresher IOCW were wrapped  
 435 around the strong mesoscale eddies, and around the submesoscale lens (cyan profile, bottom panel of  
 436 figure 8). These structures presented no front in density but a marked one in spice (see figure 6). Smith  
 437 and Ferrari (2009) suggested that these filaments could result from the stirring by the mesoscale eddies.  
 438 The slope of the fresher injections around the anticyclone A2 (on the AS section on figure 6) are compared  
 439 with the  $f/N$  ratio, and with the strain over shear ratio induced by the eddies.

440 The isospice slope varies from  $3 \cdot 10^{-3}$  to  $4 \cdot 10^{-3}$ ,  
 441  $-f/N$  from  $6 \cdot 10^{-3}$  to  $7 \cdot 10^{-3}$ ,  
 442  $-(dU/dx)/(dU/dz)$  from  $3 \cdot 10^{-3}$  to  $4 \cdot 10^{-3}$ .

443 This suggests that stirring could produce these tilted layers. Furthermore, the presence of these colder  
 444 and fresher injections below warmer and saltier PGW water could favor double diffusion.

## 445 6 Discussion and Conclusion

446 The Phys-Indien experiment took place in March 2011, in the Arabian Sea and in the Sea of Oman,  
 447 during the spring inter monsoon. The surface dynamics was dominated by mesoscale eddies along the  
 448 western coast of the Arabian Sea. A strong mesoscale anticyclone was observed in the eastern part of the  
 449 Sea of Oman, characteristic of the spring inter monsoon. These eddies are observed on the monthly sea  
 450 level climatologies from satellite altimetry with the same sizes, but with a stronger intensity in 2011, in  
 451 particular the cyclone south of Ra's Al Hadd. Nevertheless the eddies from March 2011 showed surface  
 452 velocities comparable in intensity with the HYCOM model used in L'Hégaret et al. (2015).

453 Vertical sections of velocities, obtained with a VM-ADCP, showed that these energetic mesoscale  
 454 eddies have a deep dynamical influence; they uplift of downlift the water masses below them (IOCW and  
 455 PGW). Inside the cores of these eddies, these water masses retain the thermohaline characteristics they  
 456 had at the time of their trapping. PGW filaments wrapping around these eddies are subject to mixing.  
 457 Besides, tilted layers, primarily of cold and fresh IOCW, are observed around the eddies; this can induce  
 458 mixing and dilution of the highly saline waters.

459 In the western Sea of Oman, the PGW outflow appears fragmented, forming small eddies, filaments  
 460 and a few isolated patches. Two layers of PGW, with different densities, from the winter monsoon and  
 461 earlier mixed PGW, were observed at the same location, due to the anticyclonic recirculation of PGW  
 462 in the western basin. The PGW outflow was not observed in the measurements along the coast between  
 463 Ra's Al Hamra and Ra's al Hadd, with the exception of a few small coastal patches; most of PGW  
 464 was advected north, around anticyclones A1 and A3, slowly diluting along its pathway, with a salinity

below 37 psu. A similar situation was observed on the HYCOM simulation from L'Hégaret et al. (2015) (figures 21 and 22) with an ejection at Ra's Al Hamra with a difference of 0.6 psu between the front of the ejection and the surrounding waters, comparable with the observations from the SeaSoar. Also, a coastal branch of PGW was found on the model between Ra's Al Hadd and Ra's Al Hamra, with a salinity up to 36.8 psu, as observed on the profiles from March 2011.

A submesoscale lens recorded off Ra's Al Hadd possessed strong salinity (over 37 psu) and temperature, characteristic of the winter monsoon. Different hypotheses were proposed for its formation; most likely, this lens can have been formed by the fragmentation of the PGW outflow, by the mesoscale eddies, at Ra's Al Hamra, 15 days before the sampling of the lens. This submesoscale lens was located between two mesoscale eddies during the Phys-Indien experiment, and had an elliptical structure. These mesoscale eddies deformed the lens, making it unsteady, and float trajectories suggest that it rapidly disappeared afterwards. The shear and strain of the mesoscale eddies which contributed to form the lenses also lead to their disappearance.

Thus, spring presents favourable conditions for PGW lens detection, with their ejection from the coastal outflow, and their advection around mesoscale eddies. During the summer monsoon, the PGW outflow is expelled by the Ra's Al Hadd jet, an intense mesoscale dipole, which may form but also disrupt PGW lenses.

In March 2014, a second Phys-Indien experiment took place around the Arabian Peninsula; the comparison between the results of the two experiments will be the subject of a forthcoming study.

## 7 Acknowledgements

Pierre L'Hégaret thanks DGA (French Ministry of Defence) and the Brittany Region for his PhD grant. Xavier Carton acknowledges support from ANR DGA under the Synbios project of the Astrid program.

## References

- Al Saafani, M., Shenoi, S., Shankar, D., Aparna, M., Kurian, J., Durand, F., and Vinayachandran, P. (2007). Westward movement of eddies into the gulf of aden from the arabian sea. *Journal of Geophysical Research: Oceans (1978–2012)*, 112(C11).
- Banse, K. (1997). Irregular flow of persian (arabian) gulf water to the arabian sea. *Journal of marine research*, 55(6):1049–1067.
- Barth, J. A., O'Malley, R. T., Fleischbein, J., Smith, R. L., Huyer, A., et al. (1996). SeaSoar and ctd observations during coastal jet separation cruise w9408a, august to september 1994. Technical report, Corvallis, OR: College of Oceanic and Atmospheric Sciences.
- Bower, A. S. and Furey, H. H. (2012). Mesoscale eddies in the gulf of aden and their impact on the spreading of red sea outflow water. *Progress in Oceanography*, 96(1):14–39.
- Bower, A. S., Hunt, H. D., and Price, J. F. (2000). Character and dynamics of the red sea and persian gulf outflows. *Journal of Geophysical Research: Oceans*, 105(C3):6387–6414.
- Carton, X., L'Hégaret, P., and Baraille, R. (2012). Mesoscale variability of water masses in the arabian sea as revealed by argo floats. *Ocean Science*, 8:227–248.
- Chelton, D. B., Deszoeke, R. A., Schlax, M. G., El Naggar, K., and Siwertz, N. (1998). Geographical variability of the first baroclinic rossby radius of deformation. *Journal of Physical Oceanography*, 28(3):433–460.
- Findlater, J. (1969). A major low-level air current near the indian ocean during the northern summer. *Quarterly Journal of the Royal Meteorological Society*, 95(404):362–380.
- Fischer, A. S., Weller, R. A., Rudnick, D. L., Eriksen, C. C., Lee, C. M., Brink, K. H., Fox, C. A., and Leben, R. R. (2002). Mesoscale eddies, coastal upwelling, and the upper-ocean heat budget in the arabian sea. *Deep Sea Research Part II: Topical Studies in Oceanography*, 49(12):2231–2264.

- 510 Hoskins, B. (1974). The role of potential vorticity in symmetric stability and instability. *Quarterly*  
511 *Journal of the Royal Meteorological Society*, 100(425):480–482.
- 512 IOC, S. and IAPSO (2010). The international thermodynamic equation of seawater - 2010 : Calculation  
513 and use of thermodynamic properties.
- 514 Kumar, S. P. and Prasad, T. (1999). Formation and spreading of arabian sea high-salinity water mass.  
515 *Journal of Geophysical Research: Oceans (1978–2012)*, 104(C1):1455–1464.
- 516 Lee, C. M., Jones, B. H., Brink, K. H., and Fischer, A. S. (2000). The upper-ocean response to monsoonal  
517 forcing in the arabian sea: seasonal and spatial variability. *Deep Sea Research Part II: Topical Studies*  
518 *in Oceanography*, 47(7):1177–1226.
- 519 L’Hégaret, P., Duarte, R., Carton, X., Vic, C., Ciani, D., Baraille, R., and Corréard, S. (2015). Mesoscale  
520 variability in the arabian sea from hycom model results and observations: impact on the persian gulf  
521 water path. *Ocean Science Discussions*, 12:493–550.
- 522 L’Hégaret, P., Lacour, L., Carton, X., Rouillet, G., Baraille, R., and Corréard, S. (2013). A seasonal  
523 dipolar eddy near ras al hamra (sea of oman). *Ocean Dynamics*, 63(6):633–659.
- 524 Lueck, R. G. and Picklo, J. J. (1990). Thermal inertia of conductivity cells: Observations with a sea-bird  
525 cell. *Journal of Atmospheric and Oceanic Technology*, 7(5):756–768.
- 526 Meshal, A. and Hassan, H. (1986). Evaporation from the coastal water of the central part of the gulf.  
527 *Arab Gulf Journal of Scientific Research*, 4(2):649–655.
- 528 Pous, S., Carton, X., and Lazure, P. (2004). Hydrology and circulation in the strait of hormuz and the  
529 gulf of oman—results from the gogp99 experiment: 2. gulf of oman. *Journal of Geophysical Research:*  
530 *Oceans (1978–2012)*, 109(C12).
- 531 Prasad, T., Ikeda, M., and Kumar, S. P. (2001). Seasonal spreading of the persian gulf water mass in  
532 the arabian sea. *Journal of Geophysical Research: Oceans*, 106(C8):17059–17071.
- 533 Premchand, K., Sastry, J., and Murty, C. (1986). Watermass structure in the western indian ocean, part  
534 ii, the spreading and transformation of the persian gulf water. *Mausam*, 37(2):179.
- 535 Privett, D. (1959). Monthly charts of evaporation from the n. indian ocean (including the red sea and  
536 the persian gulf). *Quarterly Journal of the Royal Meteorological Society*, 85(366):424–428.
- 537 Reynolds, R. M. (1993). Physical oceanography of the gulf, strait of hormuz, and the gulf of oman—results  
538 from the mt mitchell expedition. *Marine Pollution Bulletin*, 27:35–59.
- 539 Ruddick, B. R. (1987). Anticyclonic lenses in large-scale strain and shear. *Journal of Physical Oceanog-*  
540 *raphy*, 17(6):741–749.
- 541 Senjyu, T., Ishimaru, T., Matsuyama, M., and Koike, Y. (1998). High salinity lens from the strait of  
542 hormuz. *Offshore Environment of the ROPME Sea Area after the War-Related Oil Spill*, pages 35–48.
- 543 Smith, K. S. and Ferrari, R. (2009). The production and dissipation of compensated thermohaline  
544 variance by mesoscale stirring. *Journal of Physical Oceanography*, 39(10):2477–2501.
- 545 Swift, S. A. and Bower, A. S. (2003). Formation and circulation of dense water in the persian/arabian  
546 gulf. *Journal of Geophysical Research: Oceans*, 108(C1).
- 547 Thoppil, P. G. and Hogan, P. J. (2009). On the mechanisms of episodic salinity outflow events in the  
548 strait of hormuz. *Journal of Physical Oceanography*, 39(6):1340–1360.
- 549 Vic, C., Rouillet, G., Capet, X., Carton, X., Molemaker, M., and Gula, J. (2015). Eddy-topography  
550 interactions and the fate of the persian gulf outflow. *Journal of Geophysical Research: Oceans*.
- 551 Vic, C., Rouillet, G., Carton, X., and Capet, X. (2014). Mesoscale dynamics in the arabian sea and  
552 a focus on the great whirl life cycle: A numerical investigation using roms. *Journal of Geophysical*  
553 *Research: Oceans*, 119(9):6422–6443.

- 554 Walsh, D. (1995). A model of a mesoscale lens in large-scale shear. part i: Linear calculations. *Journal*  
555 *of physical oceanography*, 25(5):735–746.
- 556 Wang, Z., DiMarco, S. F., Jochens, A. E., and Ingle, S. (2013). High salinity events in the northern  
557 arabian sea and sea of oman. *Deep Sea Research Part I: Oceanographic Research Papers*, 74:14–24.
- 558 Wang, Z., DiMarco, S. F., Stössel, M. M., Zhang, X., Howard, M. K., and du Vall, K. (2012). Oscillation  
559 responses to tropical cyclone gonu in northern arabian sea from a moored observing system. *Deep Sea*  
560 *Research Part I: Oceanographic Research Papers*, 64:129–145.